

NORDITA - 93/81 A

RELATIVISTIC TIDAL INTERACTION OF A WHITE DWARF WITH A
MASSIVE BLACK HOLE

V.P. Frolov,^{1,2} A.M. Khokhlov,³ I.D. Novikov,^{4,5,6,7} C.J. Pethick,^{5,8}

CERN LIBRARIES, GENEVA

P00020304

P00020304

¹Theoretical Physical Institute, University of Alberta, Edmonton,
Canada T6G 2J1.

²P.N. Lebedev Physical Institute, Leninsky Prospect 53, Moscow, Russia.
³Astronomy Department, University of Texas, Austin, TX 78712.

⁴The Copenhagen University Observatory, Østervoldsgade 3,
DK-1350 Copenhagen K, Denmark.

⁵Nordita, Blegdamsvej 17, DK-2100 Copenhagen Ø, Denmark.

⁶Astro Space Center of the P.N. Lebedev Physical Institute,
Profsoyuznaja 84/32, Moscow, 117810, Russia.

⁷TAC, Blegdamsvej 17, DK-2100 Copenhagen Ø, Denmark.

⁸Department of Physics, University of Illinois at Urbana-Champaign,
1110 West Green Street, Urbana, IL 61801-3080.

Submitted to The Astrophysical Journal.

NORDITA . Nordisk Institut for Teoretisk Fysik

Blegdamsvej 17 DK-2100 København Ø Danmark

Relativistic Tidal Interaction of a White Dwarf with a Massive Black Hole.

Abstract

V.P. Frolov^{1,2}, A.M. Khokhlov³, I.D. Novikov^{4,5,6,7} and C.J.Pethick^{5,8}

1. Theoretical Physical Institute, University of Alberta, Edmonton,
Canada T6G 2J1

2. P.N.Lebedev Physical Institute, Leninsky Prospect 53, Moscow, 117924, Russia

3. Astronomy Department, University of Texas, Austin, TX 78712

4. The Copenhagen University Observatory, Østervoldsgade 3,
DK-1350 Copenhagen K, Denmark

5. NORDITA, Blegdamsvej 17, DK-2100 Copenhagen Ø, Denmark

6. Astro Space Center of the P.N.Lebedev Physical Institute,
Profsoyuznaja 84/32, Moscow, 117810, Russia

7. Theoretical Astrophysics Center, Blegdamsvej 17, DK-2100 Copenhagen Ø,
Denmark

8. Department of Physics, University of Illinois at Urbana-Champaign,
1110 West Green Street, Urbana, IL 61801-3080

We compute encounters of a realistic white dwarf model with a massive black hole in the regime where relativistic effects are important, using a three-dimensional, finite-difference, Eulerian, PPM hydrodynamical code. Both disruptive and non-disruptive encounters are considered. We identify and discuss relativistic effects important for the problem: relativistic shift of the pericenter distance, time delay, relativistic precession, and the tensorial structure of the tidal forces.

In the non-disruptive case stripping of matter takes place. In the surface layers of the surviving core complicated hydrodynamical phenomena are revealed. In both disruptive and non-disruptive encounters, material flows out in the form of two thin, S-shaped, supersonic jets. Our results provide realistic initial conditions for the subsequent investigation of the dynamics of the debris in the field of the black hole. We evaluate the critical conditions for complete disruption of the white dwarf, and compare our results with the corresponding results for non-relativistic encounters.

exceeds the acceleration due to self-gravity at the stellar surface (for their method see Laguna, Miller & Zurek 1993).

1. Introduction

This paper continues our program of studying the hydrodynamics of tidal interaction of stars with a massive black hole (BH). In our previous papers we studied the interaction of a polytropic stellar model with a massive black hole using the Newtonian approximation for the BH gravitation field (Khokhlov, Novikov & Pethick 1993a,b). The Newtonian approximation is sufficient for describing the interaction of normal stars with a black hole of mass $M_h \geq 10^6 M_\odot$ at distances of the order of the distance for tidal disruption. In this paper we are interested in the case when relativistic effects of the black hole gravity are important. This is the case when the pericentric distance from the black hole R_p becomes comparable to the BH radius, $r_g = 2GM_h/c^2$, $rg/R_p \simeq 1$. In addition, we are interested in stellar encounters when the tidal acceleration at the pericenter is comparable with the acceleration due to self-gravity at the stellar surface, $GM_h R_* / R_p^3 \simeq GM_* / R_*^2$, where R_* , M_* are the stellar radius and mass, respectively. Combining these two conditions, we can express the mass of the black hole as a function of the radius and mass of the star

$$M_h \leq 10^8 M_\odot \left(\frac{R_*}{R_\odot} \right)^{3/2} \left(\frac{M_*}{M_\odot} \right)^{-1/2}.$$

For this black hole mass both relativistic effects during the tidal interaction are important and tidal and self-gravity forces at the stellar surface are comparable. For stars with $M_* \simeq M_\odot$, $R_* \simeq R_\odot$ this formula gives $M_h \simeq 10^8 M_\odot$. For more compact stars with $M_* \simeq M_\odot$ relativistic tidal interaction of moderate strength would occur during encounters with black holes of smaller mass. Laguna, Miller, Zurek & Davies (1993) considered relativistic encounters of a polytropic stellar model with a massive black hole in the case when the tidal force substantially

In this paper we consider the tidal interaction of a realistic white dwarf model with a massive black hole. For white dwarfs, the stellar radius has a size during a moderate tidal interaction when the BH mass is $M_h \simeq 10^4 - 10^5 M_\odot$. A white dwarf orbiting around a BH can be a source of gravitational radiation in the frequency range $\simeq 1 \text{ sec}^{-1}$ that is important for future gravitational wave projects (Thorne 1987). Following the approach of our previous papers, we consider here parabolic encounters of a carbon-oxygen white dwarf (WD) of mass $0.6 M_\odot$ with a $10^4 M_\odot$ black hole, analyse the hydrodynamics of the WD matter, study the deposition of energy and angular momentum in the WD, and determine the critical conditions for tidal disruption. We want to understand how close the WD can approach a black hole without being destroyed.

The paper is organised as follows. The equations of motion of an extended test body in the Schwarzschild spacetime are presented in Sec. 2. The expressions for the relativistic tidal force are given in Sec. 3. Various relativistic effects important for the tidal interaction are identified and analysed in Sec. 4. The results of the hydrodynamical simulations of the tidal interaction of the WD with the black hole are presented in Sec. 5. Discussion and conclusions are given in Sec. 6.

2. Equations of motion

We consider an extended test body moving in the Schwarzschild spacetime with the metric

$$ds^2 = - \left(1 - \frac{r_g}{r}\right) c^2 dt^2 + \left(1 - \frac{r_g}{r}\right)^{-1} dr^2 + r^2 (d\theta^2 + \sin^2 \theta d\phi^2), \quad (1)$$

describing the gravitational field of a black hole of mass M_h ($r_g = 2GM_h/c^2$).

We choose coordinates in such a way that the trajectory of the body lies in the equatorial plane $\theta = 0$. The equation of motion of a test body in the Schwarzschild spacetime are (e.g. Novikov & Frolov 1989)¹

$$\left(\frac{d\tau}{cdt}\right)^2 = \tilde{E}^2 - \left(1 - \frac{r_g}{r}\right) \left(1 + \frac{\tilde{L}^2 r_g^2}{r^2}\right), \quad (2)$$

$$\begin{aligned} \frac{d\phi}{cdt} &= \frac{\tilde{L}^2 r_g^2}{r^2}, \\ \frac{dt}{d\tau} &= \frac{\tilde{E}}{1 - r/r_g}. \end{aligned} \quad (3)$$

Here τ is the proper time of the body, \tilde{E} and \tilde{L} are dimensionless integrals of motion which are connected with the total energy E and angular momentum L by the relations

$$\tilde{E} = E/M_* c^2, \quad \tilde{L} = L/M_* c r g, \quad (5)$$

and M_* is the mass of the test body. In what follows we consider parabolic motion for which $\tilde{E} = 1$, so trajectories are characterized by one dimensionless constant \tilde{L} . It is convenient to introduce the following notation:

$$\frac{R_p}{R_p} = \tilde{L}^2 r_g, \quad t_p = \tilde{L}^3 r_g / c, \quad \mu = \tilde{L}^{-1} = (r_g/R_p)^{1/2}, \quad (6)$$

¹ Strictly speaking, the center of mass of an extended body does not move along a geodesic. In our case, however, the difference can be neglected (Damour 1988).

$$\tau^* = \tau/t_p, \quad x(\tau^*) = r(\tau)/R_p, \quad t^* = t/t_p. \quad (7)$$

In this notation the equations of motion (2)-(4) take the form

$$\left(\frac{dx}{d\tau^*}\right)^2 = \frac{1}{x} - \frac{1}{x^2} + \mu^2 \frac{1}{x^3}, \quad (8)$$

$$\frac{d\phi}{d\tau^*} = \frac{1}{x^2}, \quad \frac{dt^*}{d\tau^*} = \frac{1}{1 - \mu^2/x}. \quad (9)$$

$$\begin{aligned} \text{We choose } \tau = 0 \text{ at the pericenter, for which} \\ r = r_p = R_p x_p, \end{aligned} \quad (11)$$

$$\text{where} \quad x_p = \frac{1}{2}(1 + \sqrt{1 - 4\mu^2}). \quad (12)$$

At this point $dx/d\tau^*$ changes sign from negative (for $\tau^* < 0$) to positive (for $\tau^* > 0$). We also choose $\phi(r^* = 0) = 0$, so ϕ is negative (positive) for $\tau^* < 0$ ($\tau^* > 0$).

The parameter $\mu = (r_g/R_p)^{1/2}$ characterises the relativistic corrections. For $\mu = 0$ the equations of motion take the non-relativistic form and R_p coincides with the radius of the pericenter in the non-relativistic problem.

The function $x(\tau^*)$ is an even function of τ^* , while $\phi(\tau^*)$ is odd. Therefore, it is sufficient to find their values for $\tau^* \geq 0$. The equations of motion can be integrated in terms of elliptic integrals. In particular, we have (for $\tau^* \geq 0$)

$$\begin{aligned} r^* &= \frac{2\sqrt{x}\sqrt{x^2 - x + \mu^2(x+2-\mu)}}{3} \\ &\quad + \frac{2}{3\sqrt{1+2\mu}} [(1-\mu^2)F(\varphi, \alpha) - (1+2\mu)E(\varphi, \alpha)], \\ \phi &= \frac{2}{\sqrt{1+2\mu}} F(\varphi, \alpha), \end{aligned} \quad (13)$$

$$\begin{aligned} \sin \varphi &= \frac{\sqrt{x^2 - x + \mu^2}}{x - \mu}, \\ \sin \alpha &= \sqrt{\frac{4\mu}{1+2\mu}}. \end{aligned} \quad (15) \quad (16)$$

3. Tidal accelerations

We specify two fields of orthonormal tetrads in order to obtain the expression for the tidal forces acting on an extended test body moving in the Schwarzschild spacetime in the most convenient form. The first tetrad, $e(\beta)$, is defined everywhere outside the black hole and is of the form

$$\begin{aligned} e(0)^\alpha \frac{\partial}{\partial x^\alpha} &= \left(1 - \frac{rg}{r}\right)^{-1/2} \frac{\partial}{\partial(ct)}, & e(1)^\alpha \frac{\partial}{\partial x^\alpha} &= \left(1 - \frac{rg}{r}\right)^{1/2} \frac{\partial}{\partial r}, \\ e(2)^\alpha \frac{\partial}{\partial x^\alpha} &= \frac{1}{r} \frac{\partial}{\partial \theta}, & e(3)^\alpha \frac{\partial}{\partial x^\alpha} &= \frac{1}{r \sin \theta} \frac{\partial}{\partial \varphi}. \end{aligned} \quad (17)$$

The other orthonormal tetrad field $\lambda(\beta)$ is defined along the geodesic trajectory representing the motion of an extended test body. We define this orthonormal tetrad by choosing it at the point of pericenter as

$$\begin{aligned} \lambda(0)^\alpha &= \frac{1}{\sqrt{xp}} e(0)^\alpha + \frac{\mu}{xp} e(3)^\alpha, & \lambda(1)^\alpha &= e(1)^\alpha, \\ \lambda(2)^\alpha &= e(2)^\alpha, & \lambda(3)^\alpha &= \frac{\mu}{xp} e(0)^\alpha + \frac{1}{\sqrt{xp}} e(3)^\alpha, \end{aligned} \quad (18)$$

and define it at other points of the trajectory by parallel propagation from the pericenter. The equation for parallel transport in a vacuum stationary black hole metric can be solved analytically (Mark 1983). For a Schwarzschild black hole one has (Luminet & Mark 1985)

$$\begin{aligned} \lambda(0)^\alpha &= \frac{1}{\sqrt{1-\mu^2/x}} \left(e(0)^\alpha + \frac{\mu}{x} e(3)^\alpha \right), & \lambda(1)^\alpha &= \cos \Psi \tilde{\lambda}(1)^\alpha - \sin \Psi \tilde{\lambda}(3)^\alpha, \\ \lambda(2)^\alpha &= e(2)^\alpha, & \lambda(3)^\alpha &= \sin \Psi \tilde{\lambda}(1)^\alpha + \cos \Psi \tilde{\lambda}(3)^\alpha, \end{aligned} \quad (19)$$

where

$$\begin{aligned} \tilde{\lambda}(1)^\alpha &= \frac{1}{\sqrt{1-r^2}} \left[\dot{r} e(0)^\alpha + e(1)^\alpha \right], \\ \tilde{\lambda}(3)^\alpha &= \frac{1}{\sqrt{1-r^2}} \frac{\mu}{x} \left[e(0)^\alpha + \dot{r} e(1)^\alpha \right] + \sqrt{1+\mu^2/x} e(3)^\alpha, \end{aligned} \quad (20)$$

$$\begin{aligned} U &= \frac{1}{2} C_{ij} X^i X^j, \\ C_{ij} &\equiv R_{\alpha\beta\gamma\delta} \lambda(0)^\alpha \lambda(i)^\beta \lambda(0)^\gamma \lambda(j)^\delta, \end{aligned} \quad (21)$$

and

$$\dot{r} = \pm \mu \sqrt{\frac{1}{x} - \frac{1}{x^2} + \frac{\mu^2}{x^3}}. \quad (22)$$

The function $\Psi = \Psi(\tau^*)$ obeys the equation

$$\frac{d\Psi}{d\tau^*} = \frac{1}{x^2 + \mu^2}, \quad (23)$$

and the initial condition is $\Psi(\tau^* = 0) = 0$. The solution of this equation can be written in terms of elliptical integrals

$$\Psi = \arctan \sqrt{x - 1 + \frac{\mu^2}{x}} + \frac{1}{\sqrt{1+2\mu}} F(\varphi, \alpha). \quad (24)$$

The tetrad is chosen in such a way that the vector $\lambda(0)$ coincides with the four-velocity vector of the body.

The geodesic line representing the motion of a test particle together with the tetrad $\lambda(\beta)$ form a comoving reference frame. We use this reference frame to describe the tidal forces acting on a star. The position of a point in the star with respect to the chosen reference frame can be described by a three-vector

$$\mathbf{X} = \sum_{i=1}^3 X^i \lambda(i). \quad (25)$$

Consider at first a test body which is formed by pressure-free matter (dust), and let $X^i = X^i(\tau)$ be the coordinates of a chosen volume element of matter in the comoving reference frame. The geodesic deviation equations (e.g. Misner et al. 1973) can be used to show that

$$\frac{d^2 X^i}{d\tau^2} = - \frac{\partial U}{\partial X^i}, \quad (26)$$

with

where $R_{\alpha\beta\gamma\delta}$ are the components of the Riemann curvature tensor calculated on the world line representing a moving body (i.e. at the origin of the comoving reference frame). The non-vanishing components of the tidal tensor C_{ij} in the comoving reference frame are (c.f. Mark 1983, Luminet & Mark 1985)

$$C_{ij} = \frac{GM}{R_p^3} \frac{1}{x^3} \sigma_{ij}, \quad (28)$$

with

$$\begin{aligned} \sigma_{11} &= 1 - 3 \frac{x^2 + \mu^2}{x^2} \cos^2 \Psi, \\ \sigma_{22} &= 1 + 3 \frac{\mu^2}{x^2}, \\ \sigma_{33} &= 1 - 3 \frac{x^2 + \mu^2}{x^2} \sin^2 \Psi, \\ \sigma_{13} &= \sigma_{31} = -3 \frac{x^2 + \mu^2}{x^2} \sin \Psi \cos \Psi. \end{aligned} \quad (29)$$

The quantities $x = x(\tau^*)$ and $\Psi = \Psi(\tau^*)$ are to be calculated on the chosen trajectory.

The tidal gravitational potential U takes a simple form in spherical comoving coordinates $\tilde{\rho}$, Θ and Φ :

$$X^1 = \tilde{\rho} \sin \Theta \cos \Phi, \quad X^2 = \tilde{\rho} \cos \Theta, \quad X^3 = \tilde{\rho} \sin \Theta \sin \Phi. \quad (30)$$

In these coordinates, the tidal potential is

$$U = \frac{1}{2} \frac{GM}{R_p^3} \frac{\tilde{\rho}^2}{x^3} \left[\sigma_1 + \frac{3\mu^2}{x^2} \sigma_2 \right], \quad (31)$$

where

$$\sigma_1 = 1 - 3 \sin^2 \Theta \cos^2 (\Phi - \Psi), \quad \sigma_2 = \cos^2 \Theta - \sin^2 \Theta \cos^2 (\Phi - \Psi). \quad (32)$$

In the presence of pressure, Eq.(25) has to be modified by the acceleration due to pressure gradient²

$$\frac{d^2 X^i}{d\tau^2} = -\frac{\partial U}{\partial X^i} + \rho - \frac{1}{\partial X^i} \frac{\partial P}{\partial X^i}, \quad (33)$$

where ρ is the mass density. This expression allows us to describe the effects of relativistic tidal forces in terms of Newtonian physics.

Our approach to the tidal field is valid when the characteristic size of a body is substantially less than the distance to the black hole. For our computations below (Sec. 5), in the worst case the size of the body is at least ten times less than this distance.

² In the extreme case when a body moving with ultra-relativistic velocity passes nearly a black hole, the body is affected by impulsive tidal acceleration. The effects of this acceleration were considered by Mashhoon & McClune (1993) in the limit when the tidal force is much larger than any other forces.

4. Relativistic effects

Relativistic effects influence the trajectory of a test body and the tensor structure of the tidal forces. To clarify these effects, we compare the motion of a test body with the parabolic velocity in relativistic and non-relativistic theories. We hold fixed the same conserved quantity in the two problems (relativistic and non-relativistic) – the angular momentum of the body, which unambiguously fixes the trajectory for the parabolic motion. The following four relativistic effects are important:

1. Relativistic shift of the pericenter distance,
 2. Relativistic time delay,
 3. Relativistic precession, and
 4. Tensorial structure of tidal forces.
1. The difference Δx_p between x_p and its non-relativistic limit, $x_{p,nr} = 1$, is
- $$\Delta x_p = -\frac{1}{2} \left(1 - \sqrt{1 - 4\mu^2} \right). \quad (34)$$
- For small μ this difference is $\Delta x_p \simeq -\mu^2$. In other words, the radial coordinate of a relativistic pericenter is smaller than the non-relativistic pericentric distance, R_p , by an amount $\Delta R_p = R_p \Delta x_p \simeq r g$.
2. In the non-relativistic limit ($\mu = 0$) the expression (13) gives

$$\tau_{nr}^* = \frac{2}{3\sqrt{x-1}}(x+2). \quad (35)$$

The difference

$$\Delta\tau^* \equiv \tau^* - \tau_{nr}^* \quad (36)$$

remains finite in the limit $x \rightarrow \infty$. In this limit

$$\Delta\tau^*(x \rightarrow \infty) \equiv \Delta\tau_\infty^* = \frac{2}{3\sqrt{1+2\mu}} [(1+2\mu)E], \quad (37)$$

where $K = K(m)$ and $E = E(m)$ are the complete elliptic integrals of the first and second kind, respectively, and

$$m = \frac{4\mu}{1+2\mu}. \quad (38)$$

For small μ

$$\Delta\tau_\infty^* \simeq \frac{3\pi}{8}\mu^4. \quad (39)$$

In other words, in the relativistic case it takes a longer time than in the non-relativistic case for a body with the same angular momentum to pass near a black hole and to return to the same initial radius. The time delay $\Delta T = 2t_p\Delta\tau^*$ is

$$\Delta T \simeq \frac{3\pi}{4} \left(\frac{rg}{R_p} \right)^{1/2} \frac{rg}{c}. \quad (40)$$

3. By relativistic precession we mean the following effect. Let a non-rotating rigid body have three orthogonal axes rigidly attached to it. The orientations of these axes in space, after a test body passes near a black hole and goes away, will differ slightly from their initial orientations. In the case under consideration this effect results in a difference of the angle Ψ , which enters Eq.(19), from the angle ϕ . The total precession angle is

$$\Delta\phi_{prec} = 2 \lim_{x \rightarrow \infty} (\phi - \Psi) = \frac{2}{\sqrt{1+2\mu}} K - \pi. \quad (41)$$

For small μ one has

$$\Delta\phi_{prec} \simeq \frac{3\pi}{4} \frac{rg}{R_p} = \frac{3\pi}{4}\mu^2. \quad (42)$$

4. The tensorial structure of tidal forces is different in the relativistic and non-relativistic cases. The tidal tensor is non-diagonal in a parallel propagated frame for both the relativistic and non-relativistic cases (see (28), (29)). This

tensor becomes diagonal in the frame $\tilde{\lambda}_1^\alpha, \tilde{\lambda}_2^\alpha = \lambda_2^\alpha, \lambda_3^\alpha$ instead of $\lambda_1^\alpha, \lambda_2^\alpha, \lambda_3^\alpha$. In the new frame the tensor σ takes the form

$$\begin{aligned}\sigma_{\tilde{1}\tilde{1}} &= -2 - 3\frac{\mu^2}{x^2}, \\ \sigma_{\tilde{2}\tilde{2}} &= 1 + 3\frac{\mu^2}{x^2}, \\ \sigma_{\tilde{3}\tilde{3}} &= 1.\end{aligned}\tag{43}$$

The extra term $3\mu^2/x^2$ which enters these relations describes relativistic effects. These effects lead to an additional increase of the tidal acceleration in the equatorial plane, without changing the acceleration in the perpendicular direction.

In the equatorial plane, the maximum effect is reached for the limiting value of μ ($\mu = 1/2$), when at the pericenter the star is stretched in the radial direction with a strength 4 times larger than that in the non-relativistic case.

$$\eta_r = \eta \left(\frac{1}{2} + \sqrt{\frac{1}{4} - \mu^2} \right)^{3/2},\tag{44}$$

where $\eta = \left(\frac{M_{wd}}{M_h} \right)^{1/2} \left(\frac{R_p}{R_{wd}} \right)^{3/2}$ is a measure of the acceleration due to self-gravity of the star at the surface of the star compared with the tidal acceleration at the pericenter, for the non-relativistic encounter (Press & Teukolsky 1977).

The expression (44) takes into account the decrease of the pericentric value of the radial coordinate r in the relativistic case (see Eq.(34)). The parameters η and μ are uniquely related to the black hole mass and orbital angular momentum

$$\mu = \frac{2GM_*}{c} \frac{L}{M_h},\tag{45}$$

$$\eta = \frac{1}{\sqrt{2GM_*^{5/3} R_* M_h^{2/3}}}.\tag{46}$$

The non-relativistic limit corresponds to $c \rightarrow \infty$. In this limit $\mu \rightarrow 0$ according to Eq.(45), while Eq.(46) corresponds to encounters with different L and M_h , but with a fixed strength of the interaction at the pericenter.

We describe both the hydrodynamics of the white dwarf and its self-gravity in the framework of Newtonian physics. The corresponding equations are given in Khokhlov et al. (1993a). The white dwarf is subjected to the action of the

5. White dwarf in a relativistic tidal field

We consider a white dwarf of mass M_{wd} moving on a parabolic orbit around a black hole of mass M_h . As already mentioned in Sec.4, the trajectory is uniquely defined by specifying the BH mass M_h , and the angular momentum of the orbital motion L . To characterise the relative strength of the tidal interaction we use the dimensionless parameter

relativistic tidal acceleration field, described in Sect.3. We select the cartesian coordinate system defined by the tetrad $\lambda(\beta)$. The parameters of the tidal field in this coordinate system are functions of the radial distance r , and the angle ϕ , which are defined as functions of time by Eqs.(8)-(10). These equations are integrated simultaneously with the equations of hydrodynamics.

For the integration of the hydrodynamical equations we use an Eulerian, finite-difference, directional splitting approach, similar to that used in Khokhlov et al. (1993a,b). However, in this work we use the Godunov-like, Piecewise Parabolic method (PPM) of Colella & Woodward (1984) and Collela & Glaz (1985) to perform one-dimensional sweeps. The PPM is implemented in the code as a Lagrangian step plus remap (for further details see Khokhlov (1993)). The PPM algorithm gives substantially better spatial resolution in comparison with the previously used FCT algorithm. All computations below are performed on a $32^2 \times 128$ grid, which for similar problems provides the same accuracy as in Khokhlov et al. (1993a,b) or better.

Computations begin on a stationary grid. When the expanding star reaches the boundary, the grid begins to expand uniformly, in order to keep most of the stellar matter inside the computational domain. Symmetry with respect to the equatorial plane is assumed. The boundary conditions are reflecting for the equatorial plane, and outflow at other boundaries. Self gravity is computed by the direct FFT convolution method (Hockney & Eastwood 1988). The equation of state of the WD matter in tabular form takes into account the contributions from the ideal Fermi-Dirac gas of electrons and positrons with arbitrary degeneracy and degree of relativity, ions, and equilibrium Planck radiation (Khokhlov 1991 and references therein). A simple algorithm is implemented in the code to avoid computations of empty space. The entire code is fully vectorized and parallelized

for use on Cray computers. A typical encounter requires $\simeq 600 - 800$ time steps, which takes $\simeq 1$ CPU hour on a Cray Y-MP C90.

The WD mass is taken to be $M_{wd} = 0.64 M_\odot$, its temperature to be 10^8 K, and its composition to be equal amounts of C and O by mass. With our equation of state, the radius of the WD is $R_{wd} = 8.41 \times 10^8$ cm, the central density is $\rho_c = 4.0 \times 10^6$ g cm $^{-3}$, the central pressure is $P_c = 2.2 \times 10^{23}$ ergs cm $^{-3}$, the gravitational energy is $E_g = -1.15 \times 10^{50}$ ergs, the thermal energy is $E_t = 6.49 \times 10^{49}$ ergs, and the total energy is $E_{tot} = -5.02 \times 10^{49}$ ergs.

For the integration of the hydrodynamical equations we use an Eulerian, finite-difference, directional splitting approach, similar to that used in Khokhlov et al. (1993a,b). However, in this work we use the Godunov-like, Piecewise Parabolic method (PPM) of Colella & Woodward (1984) and Collela & Glaz (1985) to perform one-dimensional sweeps. The PPM is implemented in the code as a Lagrangian step plus remap (for further details see Khokhlov (1993)). The PPM algorithm gives substantially better spatial resolution in comparison with the previously used FCT algorithm. All computations below are performed on a $32^2 \times 128$ grid, which for similar problems provides the same accuracy as in Khokhlov et al. (1993a,b) or better.

Computations begin on a stationary grid. When the expanding star reaches the boundary, the grid begins to expand uniformly, in order to keep most of the stellar matter inside the computational domain. Symmetry with respect to the equatorial plane is assumed. The boundary conditions are reflecting for the equatorial plane, and outflow at other boundaries. Self gravity is computed by the direct FFT convolution method (Hockney & Eastwood 1988). The equation of state of the WD matter in tabular form takes into account the contributions from the ideal Fermi-Dirac gas of electrons and positrons with arbitrary degeneracy and degree of relativity, ions, and equilibrium Planck radiation (Khokhlov 1991 and references therein). A simple algorithm is implemented in the code to avoid computations of empty space. The entire code is fully vectorized and parallelized

for use on Cray computers. A typical encounter requires $\simeq 600 - 800$ time steps, which takes $\simeq 1$ CPU hour on a Cray Y-MP C90.

The WD mass is taken to be $M_{wd} = 0.64 M_\odot$, its temperature to be 10^8 K, and its composition to be equal amounts of C and O by mass. With our equation of state, the radius of the WD is $R_{wd} = 8.41 \times 10^8$ cm, the central density is $\rho_c = 4.0 \times 10^6$ g cm $^{-3}$, the central pressure is $P_c = 2.2 \times 10^{23}$ ergs cm $^{-3}$, the gravitational energy is $E_g = -1.15 \times 10^{50}$ ergs, the thermal energy is $E_t = 6.49 \times 10^{49}$ ergs, and the total energy is $E_{tot} = -5.02 \times 10^{49}$ ergs.

With this central density, the WD is practically non-relativistic, and is close to an $n = 1.5$ polytrope. We start the integration when the radial coordinate of the WD, r , is $r = 2r_p$. In what follows, we present our results in units in which $G = M_{wd} = R_{wd} = 1$.

We computed five encounters of the WD with a black hole of mass $M_h = 8.94 \times 10^3 M_\odot$. The main parameters of the encounters are given in Table 1. The encounters N1 to N4 are relativistic, and are characterised by different orbital angular momenta L . The non-relativistic encounter N5 was computed for comparison.

First, we consider the encounter N1 during which the star partially survives (Fig.1). At the beginning, the picture of the relativistic encounter resembles the picture of the Newtonian encounter studied in our previous papers (Khokhlov et al. 1993a,b). At first, the tide is almost static. When the WD approaches the pericenter, the tide becomes dynamic. The WD develops a typical S-shape tide (Fig.1a-1d), first discovered in simulations of Evans & Kochanek (1989). Soon after that, the tidal lobes transform into two narrow jets of material, outflowing with supersonic velocity. The bounded core of the star clearly separates (Fig.1e-1j). The inner parts of the core are in a state of visible rotation. In the outer layers of the core, strong, non-linear effects take place. First, some material from

the jets returns, and falls back onto the core. The return of matter begins approximately at a time corresponding to Fig.1f. Second, formation of rotationally supported hole-like structures, similar to that found in our non-relativistic computations, is clearly seen (Fig.1g-i). Fig.2a,b shows the total energy and angular momentum of the WD, computed on the expanding grid, and on the grid which expansion was halted at $t \approx 7$. We see that the WD continues to gain both energy and angular momentum, but both are being deposited into the jets.

Both the energy and angular momentum of the core tend to constant values, as is seen from the behaviour of E and L on the “stopped” grid. For this encounter, we estimate the stripped mass as $\approx 0.07M_{\odot}$, the remaining object has a mass $\approx 0.57M_{\odot}$, the total energy is $E \approx -2.5 \times 10^{49}$ ergs, and the angular momentum is $L \approx 3.9 \times 10^{49} \text{ g cm}^2 \text{ s}^{-1}$. Further simulations on the stopped grid show the separation of jets from the core, and the formation of a torus around the core (Fig.3). Our grid was too coarse to quantitatively follow the further evolution of the rotating object on time scales of hundreds of hydrodynamical times of the star. The structure and behavior of the torus will be studied with better resolution in the future.

The encounters N2 to N4 are disruptive. The total energy of the WD and the deposited angular momentum are given for these encounters in Table 1 for times after the passage of the pericenter when the angle to the black hole Ψ (Eq.(23)) becomes $\Psi \approx 2.4$ radian. In all cases the total energy is positive. Both the energy and angular momentum continue to increase at later times. The numbers presented in Table 1 illustrate the relative strength of the interaction. This strength increases with decreasing orbital angular momentum L . Fig.4a-c shows the results for the strongest relativistic encounter, N4. During this encounter the tidal forces dominate the flow. The main effect of the encounter is the formation of a thin, jet-like debris, expanding with supersonic velocity. The core does not

survive. Complicated hydrodynamical phenomena, which occur near the surface of the core during non-disruptive encounters, are absent here.

Fig.4d gives the results for the non-relativistic encounter N5. The orbital angular momentum for this non-relativistic encounter ($\mu = 0$) was chosen to be the same as that for the encounter N4. We compare the energy and angular momentum deposition for the relativistic and non-relativistic encounters for the moments of time, when the angle to the black hole is $\Psi \approx 2.4$ radian (Figs.3c and 3d, respectively). For these moments, the energy deposited in the WD is $\Delta E \approx 1.25 \times 10^{50}$ ergs for the relativistic case, and 9.3×10^{49} ergs for the non-relativistic case. The corresponding deposited angular momentum is $\Delta L = 1.5 \times 10^{51}$, and $9.3 \times 10^{50} \text{ g cm}^2 \text{ s}^{-1}$. The transfer is larger in the relativistic case. This is natural, since in the relativistic case the pericentric distance is smaller, the star spends more time close to the black hole, and the relativistic structure of the tidal tensor further increases the tidal acceleration (Sect.4). In our case, the decrease of the pericentric distance is $\approx 11\%$. This results in an increase of the overall coefficient in front of the expression for the tidal potential Eq.(31), proportional to $1/x^3$, by $\approx 43\%$. In addition, relativistic effects increase the components $\sigma_{\tilde{1}\tilde{1}}$ and $\sigma_{\tilde{2}\tilde{2}}$ of the tidal tensor Eq.(43) by 19% and 34%, respectively. The difference in the energy deposited in the WD in the relativistic and non-relativistic cases is consistent with these numbers. From Fig.4 we see that the S-shape is much more pronounced in the non-relativistic case. The S-shape is mainly determined by the strength of the interaction. It is more pronounced for relatively weak encounters. The other two disruptive relativistic encounters, N2 and N3, are qualitatively the same as the encounter N4 (Fig.5).

Using the data for all computed encounters we estimate the critical angular momentum of the orbital motion which separates disruptive and non-disruptive relativistic encounters to be $L_{crit} \approx 3.7 \times 10^{53} \text{ g cm}^2 \text{ s}^{-1}$. The corresponding

critical value of η , $\eta_{r,crit} \simeq 2.0$, the corresponding $\mu \simeq 0.27$. The structure of the WD considered in this paper corresponds approximately to the structure of an $n = 1.5$ polytrope. In our previous work we estimated the critical value of the parameter η as $\eta_{crit} \simeq 1.5 - 1.9$ for the disruption of the $n = 1.5$ polytrope. The fact that in the relativistic case $\eta_{r,crit} \simeq 2$ is somewhat larger than the corresponding η_{crit} for the non-relativistic case is natural. The difference in the structure of the relativistic and non-relativistic tidal tensor leads to a stronger interaction in the relativistic case (Sect.4). In addition, in the relativistic case the star spends more time near the black hole.

The fact that in the relativistic case $\eta_{r,crit} \simeq 2$ is somewhat larger than the corresponding η_{crit} for the non-relativistic case is natural. The difference in the structure of the relativistic and non-relativistic tidal tensor leads to a stronger interaction in the relativistic case (Sect.4). In addition, in the relativistic case the star spends more time near the black hole.

6. Conclusions

We have considered the encounter of a realistic white dwarf model with a massive black hole in the regime where relativistic effects are important. To describe the relativistic tidal forces, the well known approach of Mark (1983) and Mark & Luminet (1985) was used. We identified and discussed the four relativistic effects important for the problem: relativistic shift of the pericentric distance, relativistic time delay, relativistic precession, and the tensorial structure of the tidal forces. We simulated the hydrodynamics of the relativistic tidal interaction of a carbon-oxygen white dwarf of $0.64M_\odot$ with a Schwarzschild black hole of mass $8.94 \times 10^3 M_\odot$, using a three-dimensional, Eulerian, PPM hydrodynamical code. Both disruptive and non-disruptive encounters were considered.

In the non-disruptive case stripping of matter takes place. In the surface layers of the surviving core complicated hydrodynamical phenomena are revealed. In both disruptive and non-disruptive encounters, material flows out in the form of two thin, S-shaped, supersonic jets. Our results provide realistic initial conditions for the subsequent investigation of the dynamics of the debris in the field of the black hole. Kochanek (1993) has already studied the motion of the debris using the initial conditions generated in the framework of the affine model of Carter & Luminet (1986).

We evaluated the critical conditions for the complete disruption of the white dwarf. The critical angular momentum of the orbital motion is estimated as $L_{crit} \simeq 3.7 \times 10^{53} \text{ g cm}^2 \text{ s}^{-1}$. The corresponding critical η_r is $\eta_{r,crit} \simeq 2.0$. Comparison was made with the corresponding non-relativistic encounters.

Acknowledgement. This work was supported in part by the NSERC of Canada Research Grant OGP0138712, by the Danish Natural Science Council through grant 11-9640-1, by Danmarks Grundforskningsford through its support for the establishment of the Theoretical Astrophysics Center, by the US National Science Foundation grants PHY 91-00283 and AST 9115143, by NASA grants NAGW-1583 and NAGW-2975, and by the Texas Advanced Research Program. Computations were performed on the Cray Y-MP C90 of the Pittsburgh Supercomputer Center (grant AST 9300P), and on the Cray Y-MP 8/864 at the Center for High Performance Computing at Austin, Texas. A.K is grateful to NORDITA for support and hospitality during the period when the writing of this paper was completed. He also acknowledges useful discussions with J.Craig Wheeler.

References

- Carter, B. & Luminet, J.-P. 1983, A&A, 121, 97
- Colella, P. & Woodward, P.R. 1984, J.Comp.Phys., 54, 174
- Colella, P. & Glaz, H.M. 1985, J.Comp.Phys., 59, 264
- Damour, T. 1987, in *Three Hundred Years of Gravitation*, ed. S.W.Hawking & W.Israel (Cambridge University Press: Cambridge), p.129
- Evans, C.R. & Kochanek, C.S. 1989, ApJ, 346, L13
- Hockney, R.W. & Eastwood, J.W. 1988, *Computer simulations using particles* (Hilger: Bristol)
- Klychkov, A.M. 1991, A&A, 245, 114
- Klychkov, A.M. 1993, ApJ, 000, L00
- Klychkov, A.M., Novikov, I.D. & Pethick, C.J 1993a, ApJ, 418, 163
- Klychkov, A.M., Novikov, I.D. & Pethick, C.J 1993b, ApJ, 418, 181
- Kochanek, C.S. 1993, ApJ, submitted
- Laguna, P., Miller, W.A., Zurek, W.H. & Davies, M.B. 1993, ApJ, 410, L83
- Laguna, P., Miller, W.A. & Zurek, W.H. 1993, ApJ, 404, 678
- Luminet, J.P. & Mark, J.A. 1985, MNRAS, 212, 57
- Mark, J.A. 1983, Proc.Roy.Soc.Lond., A385, 431
- Mashhoon, B. & McClune, J.C. 1992, preprint, University of Missouri-Columbia

Misner, C.W., Thorne, K.S. & Wheeler, J.A. 1973, *Gravitation* (Freeman & Co: San Francisco)

Novikov,I.D. & Frolov,V.P.1989, *Physics of Black Holes* (Kluwer Academic Publishers: Dordrecht)

Press, W.H. & Teukolsky, S.A. 1977, ApJ, 213, 183

Thorne, K.S. 1987, in *Three Hundred Years of Gravitation*, ed. S.W.Hawking & W.Israel (Cambridge University Press: Cambridge), p.330

Table 1

N	μ	η_r	η	$\frac{L}{10^{53} \text{ gcm}^2 \text{s}^{-1}}$	$\frac{E_{tot}}{10^{49} \text{ ergs}}$	$\frac{\Delta L}{10^{50} \text{ gcm}^2 \text{s}^{-1}}$
1	0.267	2.22	2.51	3.8	-0.67	0.9
2	0.283	1.86	2.14	3.6	3.2	2.1
3	0.300	1.50	1.76	3.4	6.6	3.8
4	0.316	1.25	1.50	3.2	7.6	5.2
5	0.000	—	1.50	3.2	3.5	2.1

Values of E_{tot} and ΔL are given at the moments of time when the angle to the black hole is $\Psi \simeq 2.4$ radian.

thick line in each frame indicates the direction to the black hole. Times corresponding to various frames are 55.99 (frame *a*), 64.86 (*b*) and 73.92 (*c*).

Figure captions

Fig. 1.— Density contours in the equatorial (X-Y) plane, and the velocity field for the encounter N1. The time step number, and the velocity scale are shown in the upper left corner of each frame. The innermost contour corresponds to 90% of the central density, and at successive contours the density decreases by a factor of 2. The short thick line in each frame indicates the direction to the black hole. Frames are obtained in two runs with different spatial resolution. Frames *a-e* are computed on the uniformly expanding grid. Frames *f-j* are computed on the grid the expansion of which was stopped in order to get better resolution of the stellar core. The frame *j* belongs to the first run, and shows the geometry of the jets at the end of the computations. The core is not well resolved in this frame. The two last frames, *l* and *k*, show the density contours and the velocity field in the Y-Z and X-Z planes, passing through the center of the star, for the moment of time corresponding to frame *f*. Times corresponding to the various frames are -4.87 (frame *a*), 0 (*b*), 1.35 (*c*), 3.24 (*d*), 5.34 (*e*), 8.18 (*f*), 12.52 (*g*), 15.34 (*h*), 17.62 (*i*) and 38.95 (*j*).

Fig. 2.— Total energy (*a*) and angular momentum of the WD (*b*) as functions of time. Solid lines – computed on the expanding grid. Dashed lines –

computed on the grid the expansion of which was stopped at $t \approx 7$.

Fig. 3.— Density contours in the equatorial (X-Y) plane, and the velocity field for the encounter N1 computed on the stopped grid at late times. The time step number, and the velocity scale are shown in the upper left corner of each frame. The innermost contour corresponds to 90% of the central density, and at successive contours the density decreases by a factor of 2. The short

Fig. 4.— Density contours in the equatorial (X-Y) plane, and the velocity field for the relativistic encounter N4 (*a-c*), and non-relativistic encounter N5 (*d*). The time step number, and the velocity scale are shown in the upper left corner of each frame. The innermost contour corresponds to 90% of the central density, and at successive contours the density decreases by a factor of 2. The short thick line in each frame indicates the direction to the black hole. Both encounters are disruptive, and they were computed on a

uniformly expanding grid. Times corresponding to various frames are -0.71 (frame *a*), 1.40 (*b*), 15.01 (*c*) and 19.81 (*d*).

Fig. 5.— Density contours in the equatorial (X-Y) plane, and the velocity field for the relativistic encounter N2 (*a*) and N3 (*b*). The time step number, and the velocity scale are shown in the upper left corner of each frame. The innermost contour corresponds to 90% of the central density, and at successive contours the density decreases by a factor of 2. The short thick line in each frame indicates the direction to the black hole. Both encounters are disruptive. The computations performed on a uniformly expanding grid. Times corresponding to the frames are 14.14 (frame *a*) and 17.67 (*b*).

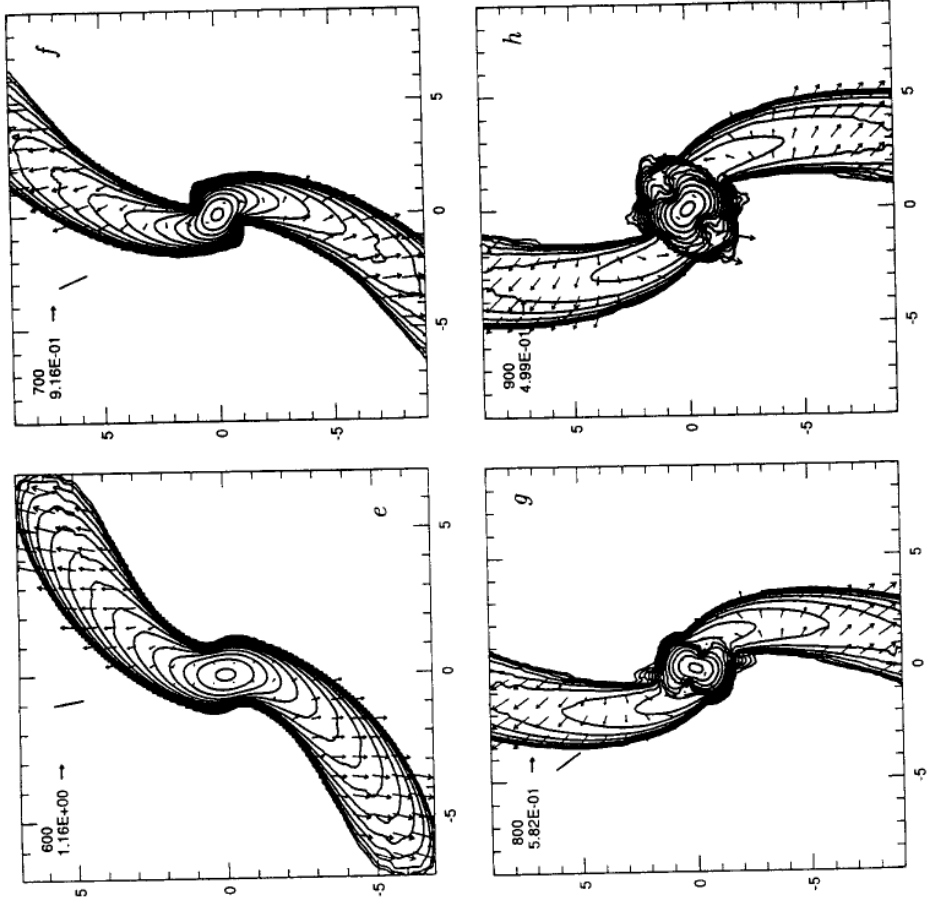


Figure 1.
Continuation

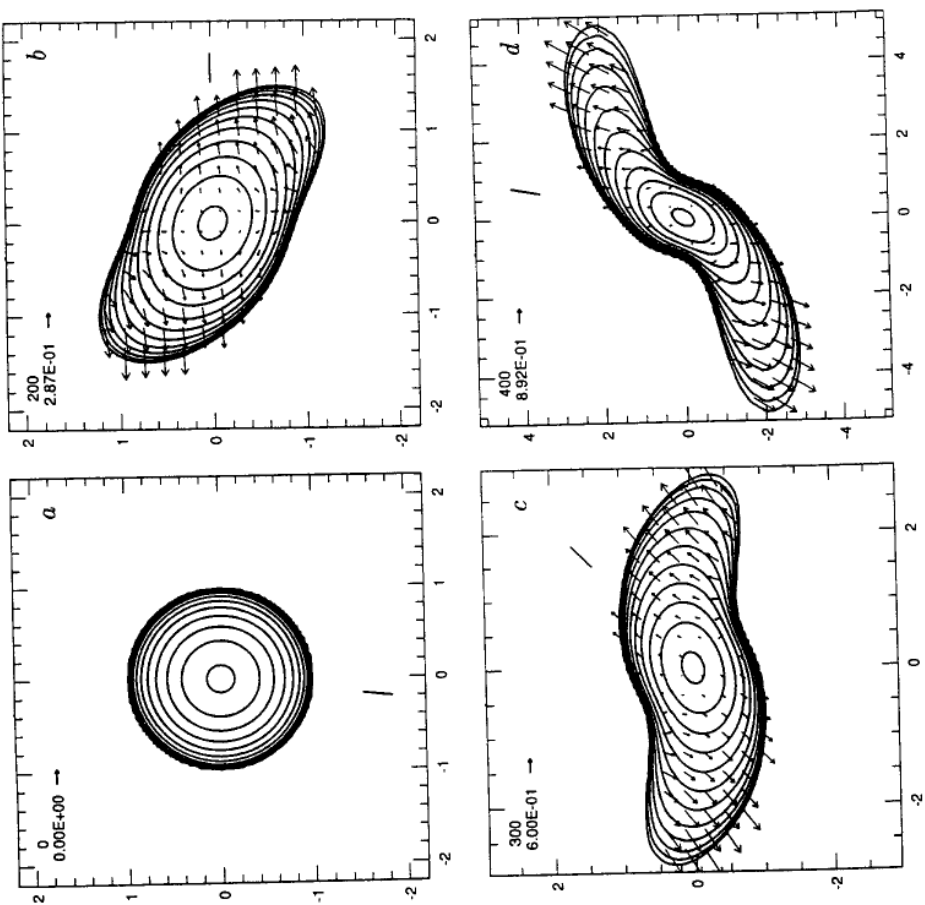


Figure 1.

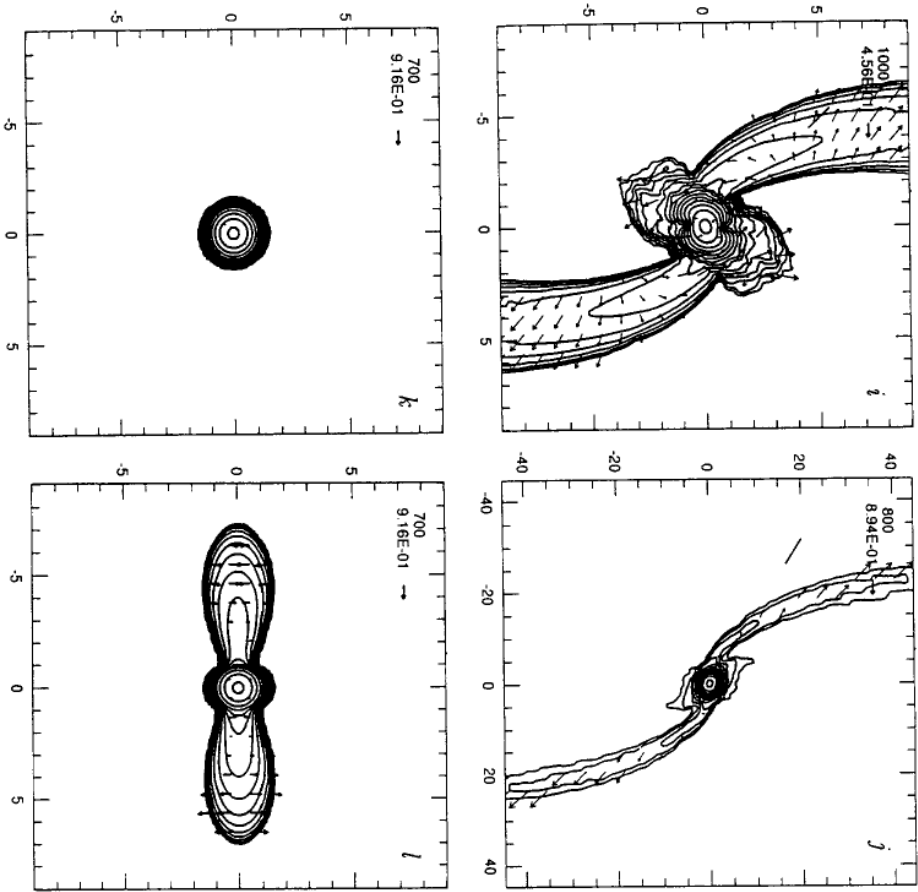


Figure 1.
Continuation

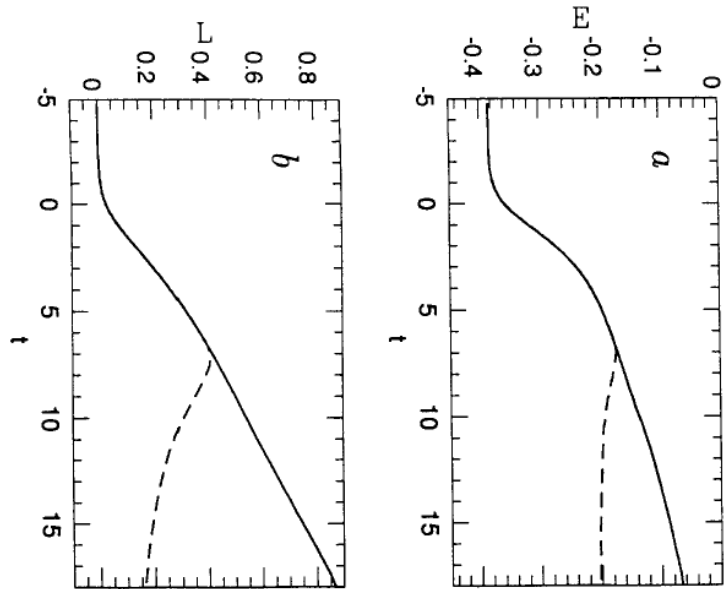


Figure 2.

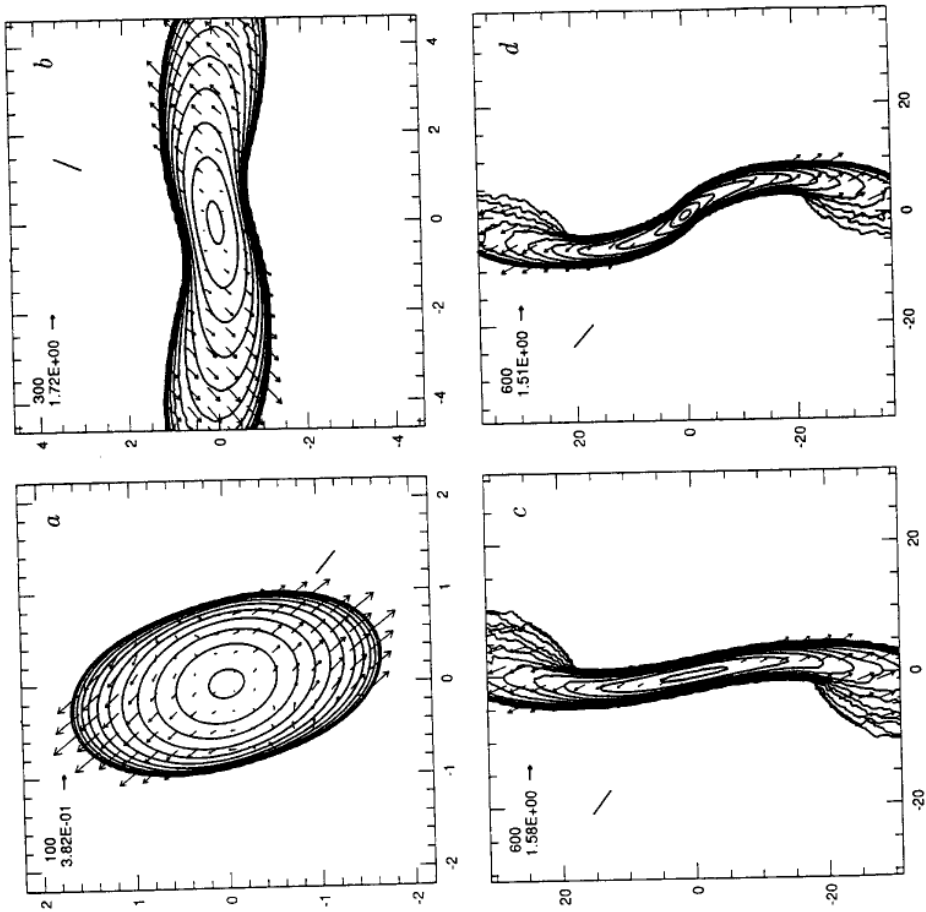


Figure 3.
5

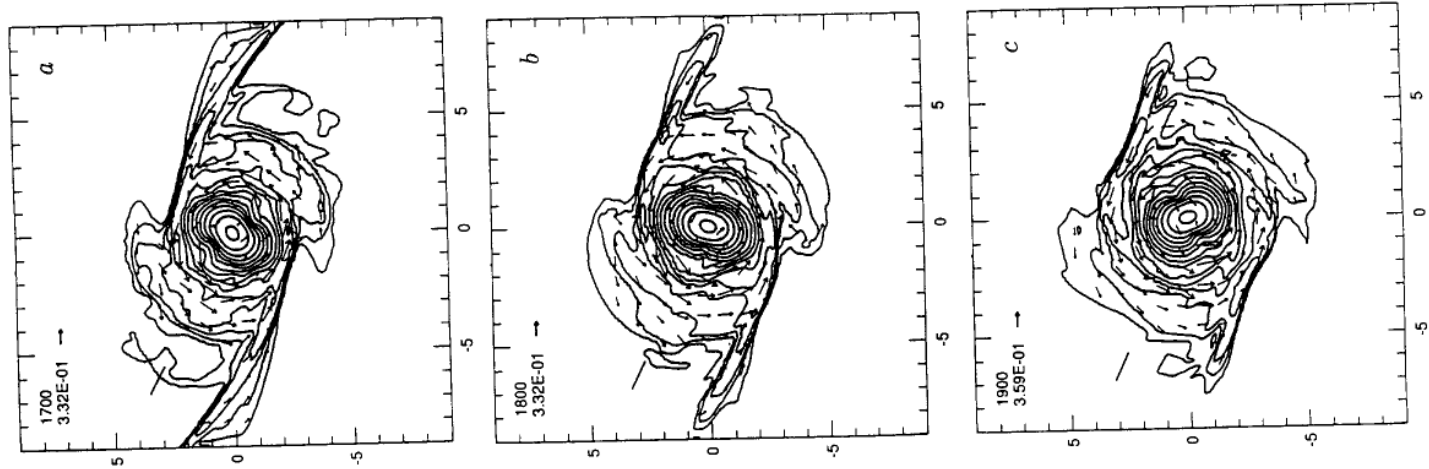


Figure 4.

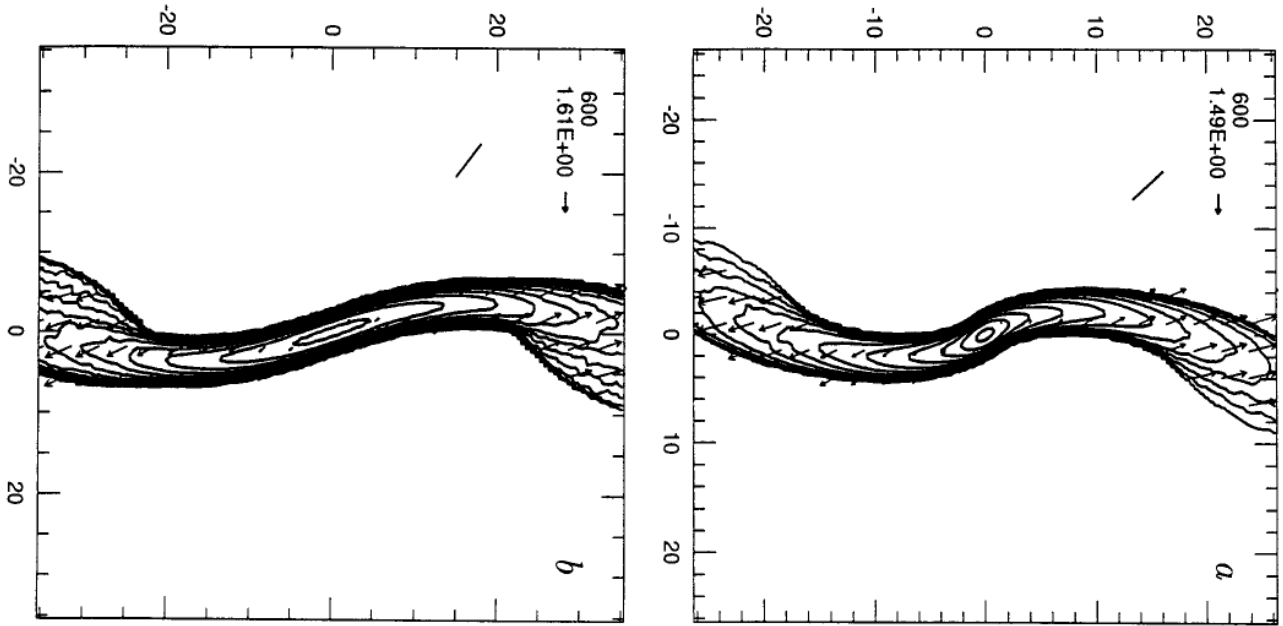


Figure 5.

